TOPICAL REVIEW • OPEN ACCESS

Physics of laser-driven tin plasma sources of EUV radiation for nanolithography

To cite this article: Oscar O Versolato 2019 *Plasma Sources Sci. Technol.* **28** 083001

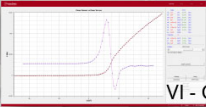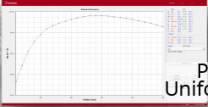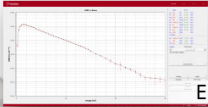View the article online for updates and enhancements.

Topical Review

Physics of laser-driven tin plasma sources of EUV radiation for nanolithography

Oscar O Versolato

Advanced Research Center for Nanolithography (ARCNL), Science Park 106, 1098 XG Amsterdam, The Netherlands

E-mail: versolato@arcnl.nl

CrossMark

Abstract

Laser-produced transient tin plasmas are the sources of extreme ultraviolet (EUV) light at 13.5 nm wavelength for next-generation nanolithography, enabling the continued miniaturization of the features on chips. Generating the required EUV light at sufficient power, reliability, and stability presents a formidable multi-faceted task, combining industrial innovations with attractive scientific questions. This topical review presents a contemporary overview of the status of the field, discussing the key processes that govern the dynamics in each step in the process of generating EUV light. Relevant physical processes span over a challenging six orders of magnitude in time scale, ranging from the (sub-)ps and ns time scales of laser-driven atomic plasma processes to the several μs required for the fluid dynamic tin target deformation that is set in motion by them.

Keywords: laser-produced plasma, plasma source of extreme ultraviolet (EUV) light, highly charged ions, spectroscopy, plasma expansion, opacity

1. Introduction

Highly charged tin ions are the atomic sources of narrow-band extreme ultraviolet (EUV) light at 13.5 nm wavelength for next-generation nanolithography that is currently poised to enter high-volume manufacturing. These highly charged ions are produced in laser-driven transient dense plasmas. The step towards using EUV light is crucial to the continuation of the miniaturization of the features on chips as represented by Moore's law [1, 2]. This law predicts that the number of transistors on an affordable CPU doubles every two years. It has been driving the semiconductor industry for more than five decades [3, 4]. A crucial step in the manufacturing of chips is photolithography [5, 6], a photochemical process where a layer of photoresist is exposed to light through a mask with a specific structure. Present-day lithography technology uses 193 nm light. The shorter the wavelength, the

better the resolution, therefore much smaller features can be printed with EUV light. Generating this EUV light at sufficient power, within the narrow 'in-band' 2% bandwidth around 13.5 nm that can be reflected by multilayer optics [7, 8] (see figure 1) presents a formidable, continuing challenge to both industry and science.

There are two crucial requirements for EUV light sources [9–11]. First, they should have high conversion efficiency (CE). CE is defined as the ratio of in-band EUV light emitted into a half-sphere backwards towards the laser (covered by the light collection optics, see figure 1) over the energy used to obtain it. Second, the plasma should create manageable amounts of debris comprising, e.g. fragments or high-energy particles that could limit optics lifetime. The method of choice for generating the required 13.5 nm EUV light is plasma emission from highly charged ions. The three most promising candidate elements were Li, Sn and Xe, all of which have ions with strong resonance transitions within the required bandwidth. However, for several reasons the obtained conversion efficiencies of Li- and Xe-based plasma sources trail those from Sn-based plasma by sizable margins [10]. Near 13.5 nm wavelength, the EUV spectrum of Sn highly charged ions is
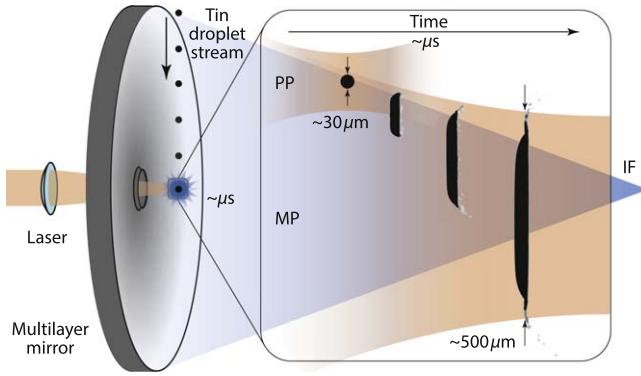
Figure 1. Simplified schematics of the laser-droplet interaction in a typical industrial EUV light source module. A spherical liquid tin microdroplet is hit by a laser prepulse (PP). The droplet is propelled by the plasma created by the PP and gets reshaped into an extended disk-shaped target suitable for the main-pulse (MP) laser irradiation, creating the highly-ionized, EUV emitting tin plasma. A multilayer mirror collects the in-band EUV light emitted in the laser-facing hemisphere and focuses it towards the so-called intermediate focus (IF).

Figure 2. Historical EUV power-scaling trend using CO_2-laser-produced plasma sources. All data points show the dose-controlled in-band EUV power at the intermediate focus of the source module (see figure 1). Reproduced with permission [17].

dominated by intense unresolved transition arrays (UTAs [12]) arising mainly from the resonance transitions $4p^6 4d^m - 4p^5 4d^{m+1} + 4d^{m-1} 4f$ in Sn^{8+}–Sn^{14+} [13] although other more highly excited states may also significantly contribute [14]. Several UTAs from strongly interacting configurations over a range of Sn charge states serendipitously contribute to the remarkably efficient production of in-band EUV radiation for next-generation nanolithography.

High power densities are required to obtain the $\sim$20–40 eV plasma temperatures to produce the highly charged Sn ions. This temperature requirement can be understood through the Stefan–Boltzmann law $j^* = \sigma_{SB} T^4$ describing the energy emitted per second per unit surface by a black body j^* as a function of temperature T; σ_{SB} is the Stefan–Boltzmann constant. Taking a representative $\sim$1 mm^2 emitting area, a prohibitively high 10^8 W power level is needed for any sustained emission. This power level necessitates plasma sources of a pulsed nature [10]. Prominent examples are discharge- and laser-produced plasma (LPP) [10]. It was the promise of power scalability that has led to the adoption of LPP by the industry [11]. Early in the development of LPP sources it was realized that the total mass of target material used during the laser-plasma interaction would need to be limited to minimize the generation of debris, e.g. in the form of target fragments or fast ions, to avoid that optics lifetime is a limiting factor in the overall availability of an EUV lithography scanner (see [10, 11] and references therein). A stream of, naturally mass-limited, liquid tin droplets was chosen to sustain the high $\sim$100 kHz repetition rate, high-power operation required for high-volume manufacturing. After a steep ramp in performance (see figure 2), such machines currently produce over 250 W of dose-controlled in-band EUV radiation [11, 15, 16]. In those state-of-the-art industrial EUV light sources, the EUV-emitting LPP is produced from liquid tin microdroplets in two steps.
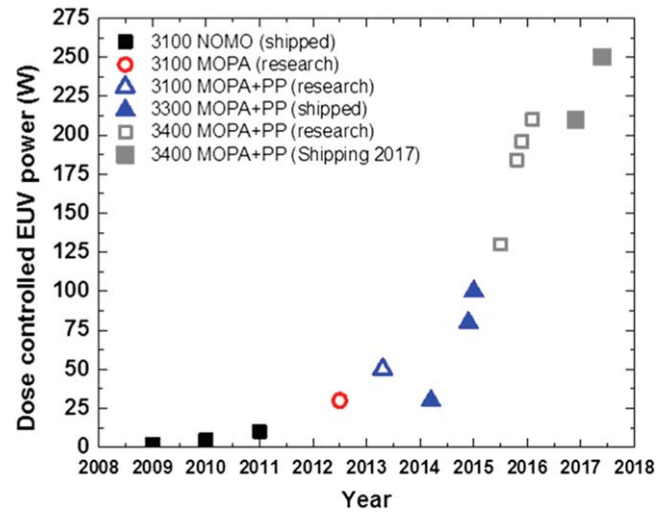
First, a low-energy prepulse (section 2) sets in motion the deformation of a tin droplet into a target shape that is suitable for interacting with the subsequent main pulse. There are two quite distinct classes of prepulses. The first class (section 2.1) is that of relatively long ($\sim$10–100 ns) laser pulses creating a quasi-stationary, strongly radiating plasma ablation front that leads to the propulsion [18, 19] and the sought-after deformation of the droplet [20–23]. In the second class (section 2.2) a high-intensity prepulse is applied on a timescale that is several orders of magnitude shorter than the time scale ($\sim$10 ns) on which pressure waves travel through the droplet. The laser-impact produces strong pressure waves that are focused in the center of the droplet due its curvature. This focusing may lead in some spectacular cases to explosive expansion and fragmentation of the target material [24–29].

Second, a high-energy laser main pulse (section 3) creates dense plasma from the liquid target that was prepared by the prepulse. In industrial sources (see figure 2) drive laser light is obtained from high-power CO_2-gas lasers that operate at 10 μm wavelength. Solid-state Nd:YAG laser systems, operating at a much shorter 1 μm wavelength could potentially provide an attractive alternative [30]. The critical density of the plasma electrons, relevant for the absorption of laser light through the process of inverse bremsstrahlung (IB), reaches levels of 10^{19} cm^{-3} (for CO_2-laser driven plasma) to 10^{21} cm^{-3} (for YAG) at the required $\sim$20–40 eV temperatures (section 3.2). These LPPs occupy a unique place in the plasma world, somewhere between the density and temperature conditions of the solar core and those of lightning. Of industrial relevance is only the EUV emission in a 2%-bandwidth around the 13.5 nm wavelength that is most efficiently reflected by available multilayer optics. Understanding the spectrum of the emitted light, and thus the complex atomic structure of highly charged Sn^{q+} ions (section 3.1) is crucial to be able to optimize source performance (section 3.3). Absorbed laser energy that does not contribute

to EUV emission may generate fast ionic and neutral debris. Ions in the unconfined, expanding plasma typically reach kinetic energies of several keV and ion kinetic energy distributions may exhibit long tails towards even higher energies (section 4). The impact of such energetic particles would affect the performance of light collecting multilayer optics. As such, plasma expansion and the generation of energetic particles is a subject of particular interest [9, 31–35].

This review builds on a review from 2011 on the topic by Banine *et al* [9]. It will combine an overview of relevant recent literature with discussions of key processes that govern the dynamics in each step in the process of generating EUV light.

2. Prepulse: laser-droplet interaction for target preparation

Current industrial EUV sources are based on the irradiation of micrometer-sized droplets of molten tin. The idea behind using such droplet streams is that each individual droplet target acts as a mass-limited target, thereby minimizing the load of debris [9, 36, 37]. Ideally, a light source is obtained that maximizes the number of in-band photons delivered per supplied tin atom. It was found early on that the pre-expansion of droplet targets is indispensable for resolving the initial mismatch between the optimal laser spot ($\sim 500\,\mu$m) and source etendue on the one hand, and the droplet diameter ($\sim 30\,\mu$m) on the other (see figure 1). This pre-expansion is accomplished by employing a relatively low-energy laser prepulse that sets in motion [38, 39] a fluid dynamic deformation [22] of the tin droplet into a suitable target shape. Such target pre-shaping is the solution adopted by the industry [11]. A distinct topic is the use of a separate laser pulse to rarefy a solid or liquid tin target in order to make a preheated plasma [40] that is to be reheated [41, 42] by a second, main, laser pulse. A detailed discussion of such rarefaction pulses lies beyond the scope of this topical review.

A precise and complete control of the velocity, size and shape of the prepulse-formed tin target is required to enable reproducible and stable maximization of CE while minimizing the amount of fragment-droplet and fast ionic debris (see e.g. [9–11, 36, 37]). Extending this control to the tilt angle of the deformed target prevents spurious back reflections of drive laser light. Such control in turn demands a thorough understanding of the laser-droplet interaction as well as the fluid-dynamic response of the droplet to the laser-pulse impact. In this section, the physics aspects of laser-droplet interaction are discussed along with the dynamics set in motion by the plasma created upon laser impact. In the available literature, two distinct classes of prepulses can be identified. Each class has its own advantages and disadvantages regarding obtainable EUV yield, and the generation of fast ionic and neutral debris. Recent developments in these two classes of prepulses are discussed in the following.

2.1. Long prepulses: from radiating steady-state ablation front to propulsion and deformation

In the first class of prepulses, relatively long (10–100 ns) laser pulses at modest intensities (10^9–$10^{12}\,\mathrm{W\,cm^{-2}}$), well above the threshold for optical breakdown and the creation of plasma are used. In the following, the time scales relevant to this problem are shown to be ordered

$$\tau_\mathrm{h} < \tau_\mathrm{a} < \tau_\mathrm{p} \ll \tau_\mathrm{i} < \tau_\mathrm{c}, \tag{1}$$

with plasma-hydrodynamic time scale τ_h, laser pulse length τ_p, liquid acoustic time scale τ_a, inertial time scale τ_i and capillary time scale τ_c. This relation illustrates the clear separation of time scales between plasma generation (τ_h, τ_p) as a cause for the propulsion and the fluid-dynamic response (τ_i, τ_c) to it. This separation of time scales facilitates the analysis of the physics problem. The laser-heated plasma has a flow length scale (the distance between droplet and critical surface) of order $R_f \sim 10\,\mu$m and the typical flow velocity is given by the speed of sound in the laser produced plasma corona, $c_\mathrm{s} \sim 10^5\,\mathrm{m\,s^{-1}}$ [43]. Flow scale and velocity imply a hydrodynamic time scale $\tau_\mathrm{h} \sim R_f/c_\mathrm{s} \sim 0.1\,$ns [43]. As the laser pulse length τ_p greatly exceeds τ_h, it creates a quasi-stationary state in the sense that the plasma ablation front only slowly varies with time [43]. The induced plasma pressure leads to propulsion of the droplet [21, 23], which sets in motion a fluid dynamic deformation of the droplet [20, 21] that is well described by incompressible flows [22]. The pressure is applied on a time scale $\sim\tau_\mathrm{p}$ that is comparable to, or longer than τ_a on which pressure waves acoustically travel (with sound speed $c \sim 2500\,\mathrm{m\,s^{-1}}$) through the droplet (with radius $R_0 \sim 25\,\mu$m), $\tau_a \sim R_0/c \sim 10\,$ns. The subsequent deformation of the droplet occurs on a much longer inertial time scale $\tau_i \sim R_0/U \sim 1\,\mu$s [20], where U is the droplet propulsion velocity. This propulsion velocity is close to the radial expansion speed [22]. The deformation typically results [22] in a thin disk type target shape (see upper two rows in figure 3) that contracts on an even longer $\sim 10\,\mu$s capillary time scale $\tau_\mathrm{c} = \sqrt{\rho R_0^3/\sigma}$, with liquid density ρ and surface tension σ [22]. The relevant time scales have thus been shown to be ordered as in equation (1).

Intriguingly, it was shown that a fully front-back symmetric deformation into a disk target (i.e. a mirror symmetry along the droplet equatorial plane with its surface normal aligned with the laser axis) can be obtained for a uniform but single-sided irradiation [22]. Related work introduced, and experimentally validated, a model describing the sensitivity of the tilt angle of the disk surface normal, as well as its size, to its relative alignment to the impacting prepulse laser light [19, 44, 45]. Further, the fluid-dynamic response of laser-impacted tin droplets was shown to be largely decoupled from the precise propulsion mechanism [21] and to be scalable to that of vaporization-accelerated millimeter-sized water droplets [20].

Still, a detailed understanding of the plasma propulsion mechanism is required to enable controlling the velocity, size and precise shape of the target. The structure of quasi-stationary ablation fronts has been extensively studied under
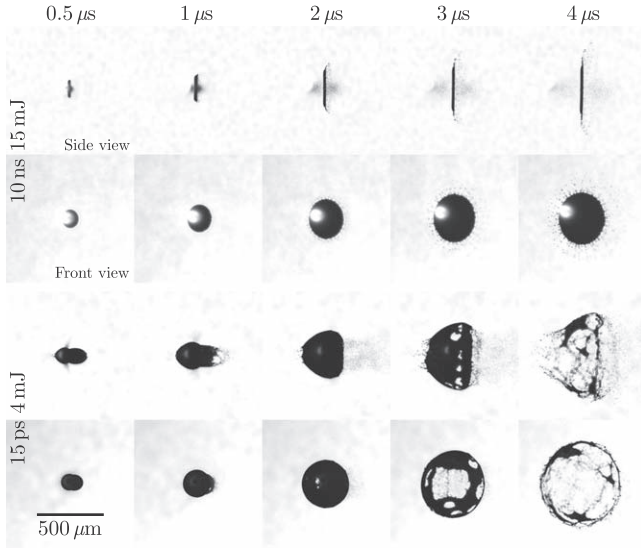
Figure 3. Stroboscopic shadowgraph images of expanding tin microdroplets taken at different time delays after laser pulse impact for two different pulse lengths (10 and 15 ps), as seen from two viewing angles (upper row: 90° side view; lower row: 30° front view). Laser impacts from the left; images are cropped and centered individually to improve visibility. A length scale bar is provided in the left-lower corner.

Figure 4. Measured propulsion velocity U of metallic microdroplets as a function of the laser energy E_{od} impinging upon the droplet. The dashed line represents a fit of a power law to the high-velocity part of the data. A fit of an offset power law, featuring the onset of propulsion, to the full data range is depicted as a solid line. Reproduced from [21].

various simplifying assumptions for several decades [46–53]. The work of Mora [50] in particular successfully describes several key processes. In many seminal works, however, the role of energy transport by thermal radiation is ignored because the studied plasma comprised light (low atomic number) elements. In the case of tin plasma, used as an EUV light source, the role of radiation transport can no longer be neglected. Recently, theoretical and experimental studies were done on the influence of radiation transport on plasma pressure in the particular case of plasmas generated from tin microdroplets [23, 25]. Remarkably, given the complexity of underlying processes, the droplet propulsion velocity turns out to be accurately described by a scaling law

$$U \sim (E - E_0)^\delta. \quad (2)$$

It accurately tracks the plasma-imparted momentum transfer over several decades of impacting laser pulse energy, E, allowing for a threshold [54–56] energy, E_0, below which no propulsion occurs (see figure 4). The power exponent δ has a value 0.60(1) for Nd:YAG [23] and 0.96(7) for CO_2 [57] laser propulsion. In the fully ablative regime, good agreement between the experiment (using a Nd:YAG laser) and simulations was obtained in [23]. The power exponent δ cannot be straightforwardly explained using any of the available analytical theories. Simulation results significantly deviate from the experimental values near the threshold energy [23]. This onset of ablation is controlled by physical processes distinct from those governing the fully ablative regime. Further work is required to fully understand the processes governing the threshold of the ablation of tin.
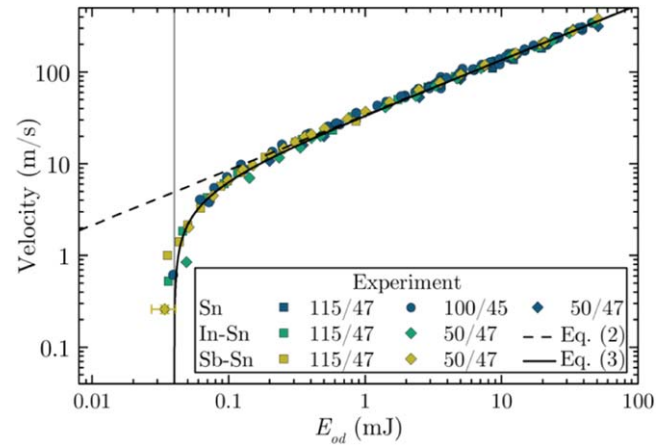
2.2. Short prepulses: from converging shock waves to cavitation and spallation

In the second class of prepulses a laser pulse is applied again with intensities typically well above the threshold for optical breakdown and plasma creation. The laser energy is absorbed by free electrons in the metallic tin, which causes the rapid heating of a thin layer of the material with a thickness well below ~1 μm [25], on the ~10 ps time scale [28] of the thermal relaxation of electron and ion subsystems. Pressure waves are generated starting from the laser-impacted region of the droplet as a result of this nearly instantaneous heating, on a time scale several orders of magnitude shorter than τ_a. These pressure waves originate from a spherical surface and converge to coincide right in the center of the droplet where they cause large tensile stress. The liquid breaks apart (cavitates) once this tensile stress exceeds the tensile strength. This cavitation triggers an explosive deformation of the droplet. Above a certain intensity threshold, the reflection of the pressure waves from the side of the droplet facing away from the laser results in violent ejection (spallation) of a thin layer of material.

The laser-droplet interaction typically results in a 3D acorn type target shape (see figures 3 and 5(b)) on a ~10 μs capillary time scale [24–27]. Recent developments [16, 58] produced tentative evidence for improved EUV source performance in terms of CE when replacing the ns-prepulse with a ps-pulse laser to produce explosive expansion, jetting [59–61] and fragmentation [27, 62]. Although some notable progress was made very recently in studies of cavitation and spallation of tin microdroplets by laser-pulse impact [24–29], further investigations are required to fully understand the key processes.

In the experiments presented in [27] for the lower laser pulse energies used, ps-ablated mass is clearly visible and seen to move away from the droplet in the direction
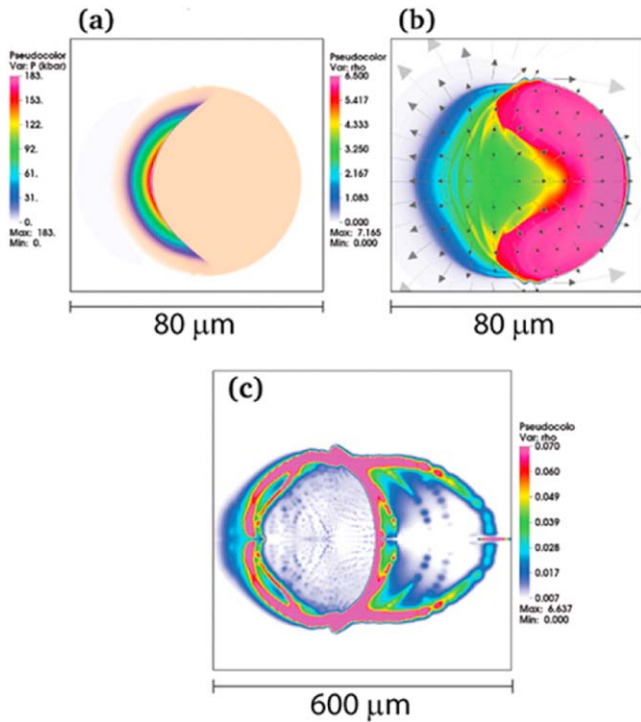
Figure 5. RALEF [63, 64] simulation results of short-pulse impact on a tin droplet (laser impinges from the left): (a) pressure distribution behind the shock front at $t = 3$ ns; (b) density distribution at $t = 23$ ns and (c) at 1 μs; arrows in (b) indicate the velocity field. Reproduced from [25]. Similar simulation results are presented in [28].

backwards towards the laser. The remarkably sharp outer boundary of this ablated mass may be explained by the existence of an inhomogeneous two-phase, gas-liquid mixture of low average density but approaching liquid density in the vicinity of the ablation front [65, 66]. In [27] the authors combined high-resolution stroboscopic shadowgraphy with an intuitive fluid dynamic model. The studies included the onset of fragmentation. In the model, the expansion of the thin tin shell is described by a simplified form of the Rayleigh–Plesset equation [67]. Good agreement between model and experimental data was found for different tin droplet sizes over a wide range of laser pulse energies [27]. In contrast to the ns laser pulse impact described above, the resulting droplet propulsion is quite limited, and is indeed much smaller than the radial expansion velocity. The dependence of this expansion velocity on the experimental parameters was shown to be captured in a heuristic single power law [27, 28].

Theoretical modeling [25, 28] has shown that there is a high sensitivity of both the rate of expansion and the morphology of the deformed droplet to the details of the equation-of-state (EOS) such as the value of the critical pressure [25]. The EOS for tin is not fully known. Results of two-dimensional simulations with the radiation-hydrodynamics code RALEF are shown in figure 5. It depicts maps of local pressure and density in a cut-out view. The target shape (density) in figure 5(c), calculated for $t = 1$ μs after laser pulse impact, resembles the corresponding experimental shadowgraphs. This resemblance indicates that the theoretical

model, with its particular choice of an EOS [25] in which negative pressures do actually not exist, provides a qualitative understanding of the cause and effects of cavitation and spallation although not yet at the accuracy required for a quantitative comparison of theory and the experimental observations. Ongoing theoretical and experimental studies undoubtedly will provide paths to further control droplet-target shaping benefiting EUV light sources.

3. Main pulse: plasma EUV emission and its spectroscopies

Once a suitable target shape is reached, the main, most energetic laser pulse is irradiated onto it. This main laser pulse transforms the liquid target into hot and dense EUV emitting plasma [11]. Highly charged tin ions Sn^{q+} are the atomic sources of EUV radiation in this transient plasma. A detailed understanding of their complex atomic structure is of paramount importance for establishing and understanding the fundamental atomic physics limitations to the CE.

3.1. Atomic structure of tin highly charged ions

The strongly correlated electronic structure [Kr] $4d^m$ ($m = 6$–0) of the highly charged open-shell ions Sn^{8+}–Sn^{14+} is particularly challenging to calculate. Spectroscopic accuracy remains inaccessible to even the most advanced *ab initio* atomic theory codes. Instead, semi-empirical methods [68, 69] based on the Cowan [70] code are employed to assess the experimentally obtained spectra in such complex systems. These 8- to 14-fold charged tin ions generate EUV light around 13.5 nm wavelength in LPP. The EUV light is generated by thousands of transitions that form UTAs [12, 71, 72]. The transition energy of these UTAs show relatively little dependence on the charge state of the ion (see figure 6) due to a serendipitous level crossing [73] involving the EUV-contributing excited configurations. For the relevant [Kr] $4d^m$ tin ions, the EUV-contributing upper configurations are, amongst others, $4p^6 4d^{m-1} 4f$, $4p^6 4d^{m-1} 5p$, and $4p^5 4d^{m+1}$. Configuration-interaction (CI) between the excited $4p^6 4d^{m-1} 4f$ and $4p^5 4d^{m+1}$ configurations is the cause of a significant redistribution of oscillator strength towards the high-energy side of the UTA, an effect referred to as spectral narrowing. Such spectral narrowing is particularly beneficial for efficient emission of in-band EUV light.

The large number of closely packed lines from these UTAs however complicates their accurate identification even when considering the contributions from a single charge state. Most dedicated spectroscopic works using, e.g. discharge sources, LPPs, or tokamaks [14, 74–84], moreover have had to deal with the emission originating from a range of tin charge states as produced in the plasma. Nevertheless, work on discharge sources provides the most accurate and complete spectroscopic data in the EUV range to date. More recently, charge-state-resolved optical spectroscopy of magnetic dipole transitions in the FLASH-electron beam ion trap (EBIT) [85] facilities at the Max Planck Institute for Nuclear Physics in
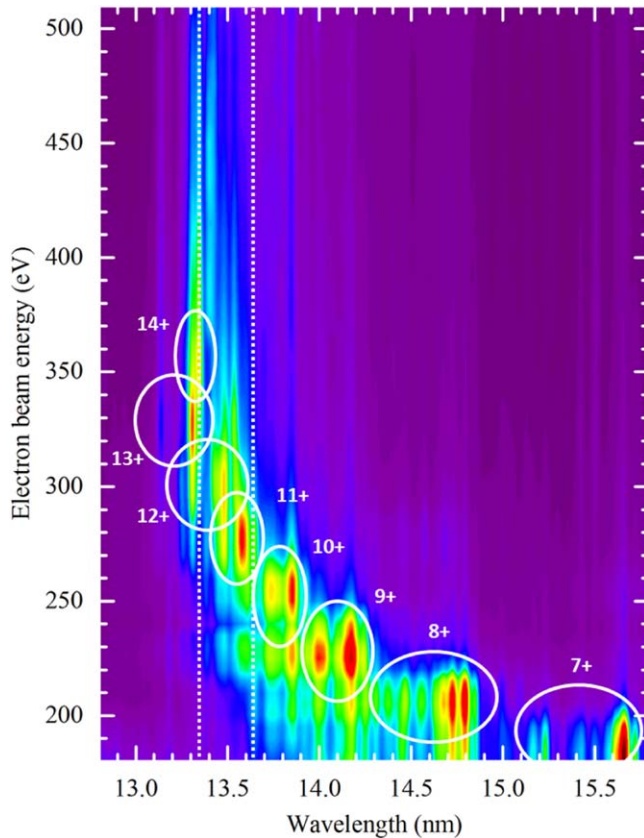
Figure 6. Spectral map of Sn ions in the EUV wavelength range as obtained from an electron beam ion trap. Its electron beam energy sets the charge state balance. The energy is stepped through at 10 V acceleration potential steps. The 2% in-band region around 13.5 nm is indicated by the white dashed rectangular outline. Resonance emission features from the tin charge states Sn^{7+} through Sn^{14+} are highlighted by white ellipsoid outlines.

Heidelberg provided a direct challenge [83, 84] to this data. The EBIT work [83, 84] suggests that line identifications in the EUV [76–79] need to be revisited. More work is required to also accurately pinpoint the EUV transitions from more highly excited states that may contribute in the emission from dense plasma.

EUV spectra obtained from laser-produced tin plasma are the product of several Sn charge states. Besides the main emission feature around 13.5 nm, the spectra contain a wealth of diagnostic information. Figure 7 shows spectra obtained from experiments where a Nd:YAG laser irradiates a tin microdroplet. The most prominent characteristic observed is the shift of the main emission feature towards the desired 13.5 nm with increasing laser intensity. This shift is related to the creation of tin ions in higher charge states. At the lower intensities, characteristic emission from the lower charge states is visible in the long wavelength region. Short-wavelength emission, between 7 and 12 nm, enables the assessment of the charge state distribution [75, 86]. Each of the tin ion's charge states has unique emission features in this wavelength range originating from radiative decay from the configurations $4p^5 4d^m 5s$ along with $4p^6 4d^{m-1} 5f$ and $4p^6 4d^{m-1} 6p$. Charge states at least up to Sn^{15+} (seen
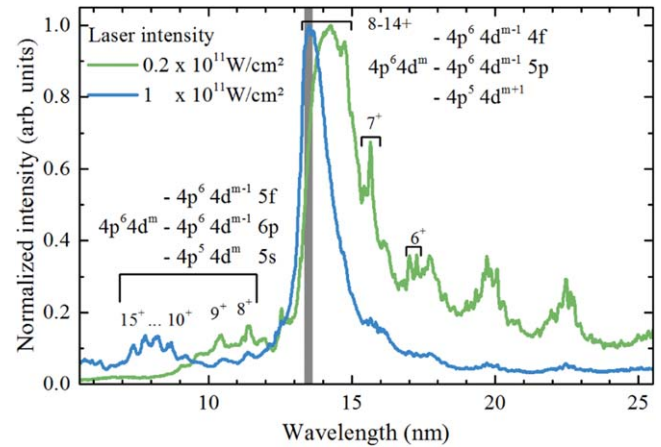

Figure 7. Emission spectra resulting from a 46 μm diameter tin droplet illuminated with a 96 μm-sized Nd:YAG laser beam at various intensities, of 15 ns duration. The gray-shaded area shows the 2% bandwidth around 13.5 nm relevant for nanolithographic applications. The emission features attributed to the various Sn ions are labeled with the respective charge state number. Also labeled are the relevant transition arrays contributing to the in-band emission and the short-wavelength features between 7 and 12 nm. (m is an integer between 0 and 6 corresponding to Sn^{14+} and Sn^{8+}, respectively.)

emitting from its excited $4p^4 5s$ configuration) are visible in the spectrum. More detailed investigations into these short-wavelength out-of-band (OOB) emission features may provide further sensitive probes into the UTA emission feature and enable monitoring, or to beneficially influence the emission by modifying laser-plasma parameters. OOB radiation in the vacuum ultraviolet to infrared spectral range emitted from plasma EUV light sources is a further topic of particular relevance for the applicability of such sources for nanolithography [87–89]. Such OOB may cause unwanted background exposure of the photoresist involved in the lithography process [90], or lead to detrimental heating of optics elements [88].

Modeling of the full laser-plasma interaction is a formidable task that requires large research teams and extensive computational capacity. Particularly challenging in the modeling of the plasma is the large range of relevant time scales, ranging over six orders in magnitude from the initial ps-duration laser-matter interaction through to the several μs needed for the ensuing fluid dynamic deformation. This large range of time scales requires the simulation problem to be cut up into several parts. Lawrence Livermore National Lab (LLNL) recently presented detailed investigations on prepulse and main pulse interactions [91]. In the Hassanein group at the Center for Materials Under eXtreme Environments at Purdue University, simulations are performed using the HEIGHTS suite of codes [10, 92, 93]. In Russia, at ISAN in collaboration with the Keldysh Institute of Applied Mathematics, several codes have been developed and maintained such as RZLine [94] and RALEF [63, 64, 95]. All these radiation-hydrodynamics simulation efforts rely on accurate opacity tables that feed into the respective codes and, thus, on
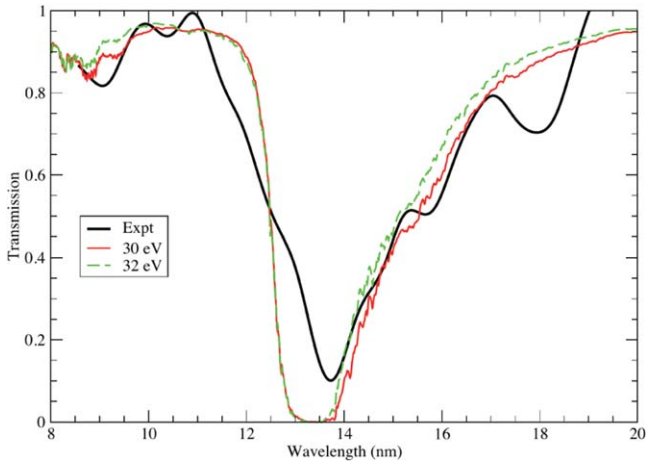
Figure 8. Comparison of the experimental data of [98] with ATOMIC calculations at various temperatures [14]. To determine the transmission, a path length of approximately 20 μm was used. Reproduced from [14].

the accurate and detailed knowledge of the atomic structure of tin.

Recently, Colgan and coworkers at Los Alamos National Lab (LANL) began a preliminary investigation into the opacity of Sn in the relevant 20–40 eV temperature range at a density of 0.01 g/cc (equivalent to a plasma electron density of $\sim 10^{21}$ cm^{-3}). In their work [14], the authors explored the accuracy of some approximations used in opacity models for the ion stages of Sn ranging from neutral through 18 times ionized. They found that the use of intermediate-coupling methods, which only retain interactions between levels from the same configuration, cannot describe the important bound-bound transitions in Sn with sufficient accuracy. Instead a full CI treatment is required to treat the strong mixing between the various $n = 4$ subshells that give rise to the $\Delta n = 0$ transitions that dominate the opacity spectrum. The required large numbers of configurations quickly become computationally daunting and hybrid calculations have had to be explored. In such hybrid calculations, full CI is retained only for the most important resonance transitions.

Local-thermodynamic-equilibrium (LTE) opacities were generated at selected temperatures and densities from the Los Alamos suite of atomic codes [96]. More specifically, they employed the ATOMIC code [97] incorporating atomic structure data computed from CATS based on Cowan's atomic structure codes, making use of chemEOS. Results were compared (see figure 8) to the experiments of Fujioka and coworkers [98] who generated an absorption spectrum of a uniform plasma using backlighting with thermal x-rays. Reasonable agreement with the measured transmission was found although the calculations exhibit a much steeper decrease in transmission at around 12 nm than was indicated in the measurements. This discrepancy is an intriguing and outstanding issue to date. Currently, to address such issues, more complete CI calculations are performed at LANL that will be compared to ongoing LPP experiments at ARCNL.

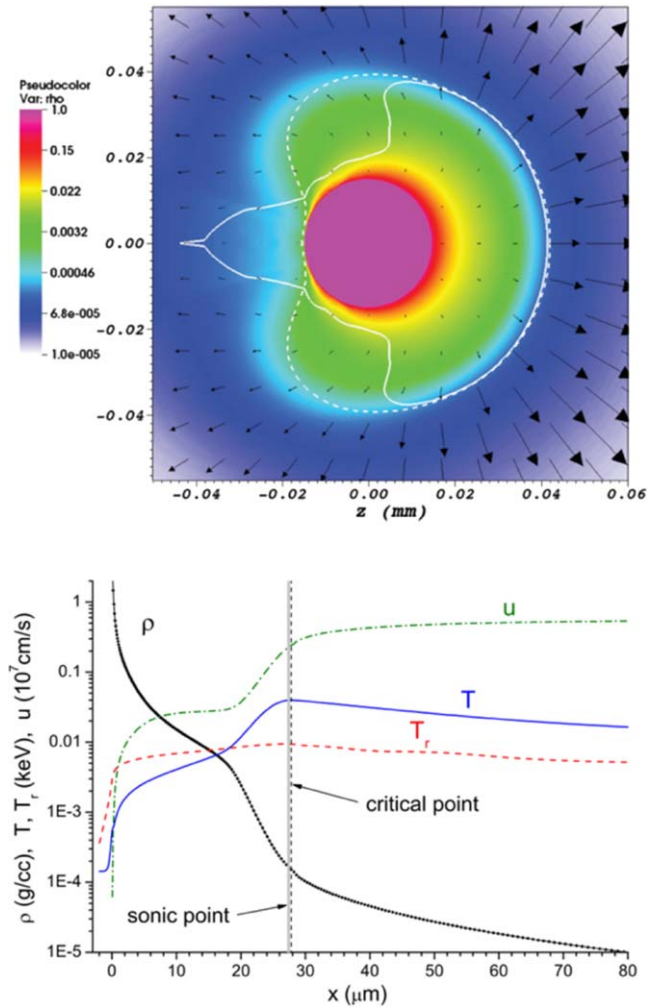Optical spectroscopic investigations on the LPP can help characterize plasma parameters [99–105] such as ion and

Figure 9. (Upper) 2D-RALEF simulation of the plasma density and velocity around a 30 μm diameter droplet of tin, irradiated from the right by a CO_2 laser pulse. The sonic surface is shown as a solid contour line; the dashed contour marks the position of the critical surface. Arrows indicate the magnitude and direction of the flow velocity; (lower) Profiles of the density ρ, velocity u, matter temperature T, and radiation temperature T_r along the laser beam propagation axis. Reproduced from [43].

electron densities and temperatures by studying the observed line strengths and their shapes. Detailed spectroscopic information on the intermediate Sn ions remains scarce. Sn^{3+} data became only recently available [106]. For Sn^{4+} line identifications are largely lacking. Time-resolved two-dimensional profiles of plasma electron density and temperature of EUV producing tin LPP were obtained [107, 108] from the ion components of collective Thomson scattering spectra in the optical domain. Imaged spectroscopy may also complement direct ion charge energy spectroscopy (see section 4) to diagnose any produced atomic or ionic debris.

3.2. Laser absorption in plasma and optical density considerations

LPP is all but stationary. It rarefies and expands rapidly into the vacuum (or buffer gas, see section 4). Its dynamics need to be considered in detail.

Figure 9 shows two-dimensional results [43] from the radiation-hydrodynamics code RALEF [63, 64] on the plasma flow patterns around a 30 μm diameter droplet of tin, irradiated from one side by a CO_2 laser pulse 10 ns in length with an intensity value typical for EUV-lithography sources, here 4×10^9 W cm^{-2}. The plasma ablation front is seen to have a quasi-stationary nature, with the structure of the ablation front only slowly varying in time. Ablation is strongly influenced by radiative losses [23, 43] as indicated in section 2.1. These radiative losses are highest from the hottest region, where the laser light is absorbed. A part of the absorbed laser energy is transported into the higher-density region by means of electron heat conduction as well as by radiation from the lower-density, coronal regions. This fraction of the energy causes laser ablation and accelerates the plasma expansion.

In this example, most of the laser light is absorbed near the critical plasma electron density n_c. This density depends on the drive laser wavelength λ [43] by the relation

$$n_c \sim \lambda^{-2}. \tag{3}$$

It sets the maximum density where the laser light can propagate. Laser light not absorbed before reaching the n_c surface is reflected from it. The industry standard for both main and prepulse is the CO_2 gas laser. Such laser systems operate at infrared wavelengths of 10 μm, so $n_c = 10^{19}$ cm^{-3}. The critical surface lies far away from the ablated tin droplet surface, at 28 μm. Laser light is mostly absorbed (approximately 70%) in a very small region near the critical surface through the mechanism of IB [43]. Other absorption mechanisms may also be made to play a role, such as resonance absorption [109, 110]. IB absorption is more efficient for shorter-wavelength drive lasers, as its cross section K, at constant temperature and away from the critical surface, scales with electron density n as [50, 111]

$$K \sim n^2 \lambda^2, \tag{4}$$

noting that allowed values for n (i.e. where the laser can penetrate) increase with decreasing drive laser wavelength $n \sim \lambda^{-2}$. Thus, very roughly the cross section may be expected to scale as $K \sim \lambda^{-2}$. Shorter-wavelength laser light is absorbed in an extended region by the IB mechanism before reaching the critical surface [50, 112, 113]. Ablation rates, the rate at which mass m is removed from the surface, also scale favorably with decreasing wavelength, typically as $\dot{m} \sim I^{5/9} \lambda^{-4/9}$ [114, 115].

These scaling relations lead to the consideration of Nd:YAG lasers. Besides having several industrially relevant advantages, its shorter 1 μm wavelength radiation would benefit the emission efficiency of the plasma through higher laser-plasma absorption.

It is instructive to compare the plasma flow patterns, and typical plasma characteristics created by the two types of laser system. Figure 10 shows simulation results [43] on the plasma flow patterns around a 30 μm diameter droplet of tin, irradiated from one side by a 1 μm wavelength laser pulse with an intensity value of 2×10^{11} W cm^{-2}. The significant
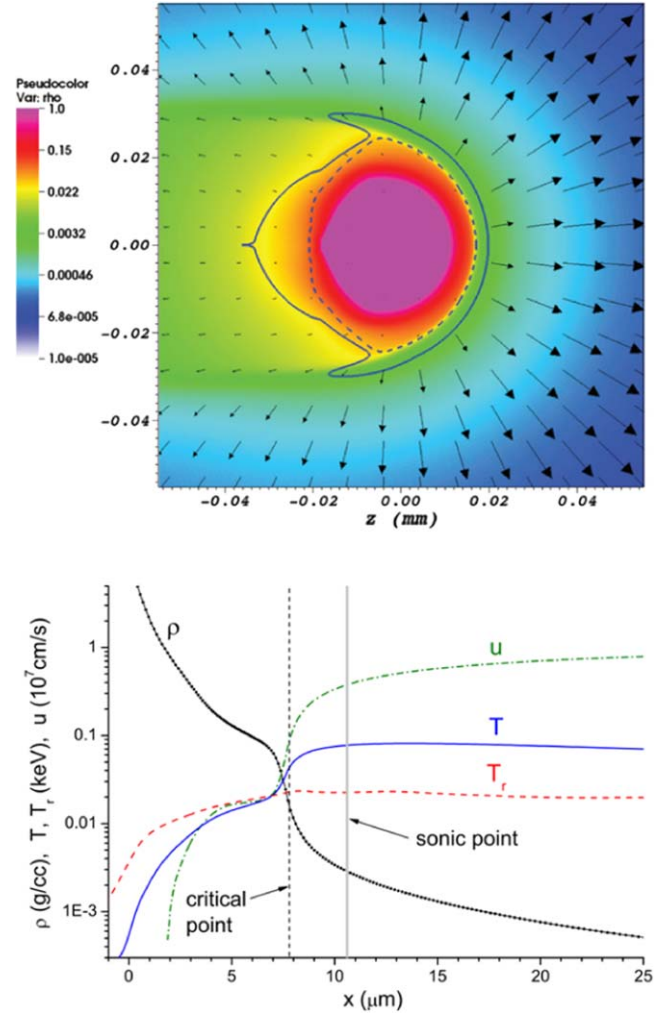

Figure 10. (Upper) 2D-RALEF simulation of the plasma density and velocity around a 30 μm diameter droplet of tin, irradiated from the right by a Nd:YAG laser pulse. The sonic surface is shown as a solid contour line; the dashed contour marks the position of the critical surface. Arrows indicate the magnitude and direction of the flow velocity; (lower) Profiles of the density ρ, velocity u, matter temperature T, and radiation temperature T_r along the laser beam propagation axis. Note the change in scales with respect to figure 9. Reproduced from [43].

increase in laser intensity I compared to the CO_2 case is required to reach the correct temperature T for the tin charge state balance; T typically scales as a power of the product $(\lambda^2 I)$ [50, 116, 117]. The average charge state scales as $\bar{Z} \sim T^{0.6}$ as derived from a thermodynamically consistent power-law approximation to the tin equation of state [43]. In figure 10 the critical surface at density $n_c = 10^{21}$ cm^{-3} lies much closer to the ablated tin droplet surface, at 8 μm. Again a quasi-stationary ablation front is established and again it is strongly influenced by radiative losses. Note that the coronal region is isothermal to a good approximation due to its high electron heat conductivity. Contrasting with the CO_2 case, the strongest radiative losses, or highest effective emissivity can be expected to occur in regions with densities below the critical one [118, 119] because of the significant absorption of

laser light in the underdense region in front of the critical surface, and strong self-absorption of radiation by the plasma (opacity).

Opacity effects on EUV emission from 1 μm-laser-driven tin plasma have been experimentally investigated by Fujioka and coworkers [98]. Their results indicate that control of the optical depth of the laser-produced Sn plasma is essential for obtaining high conversion to 13.5 nm wavelength EUV radiation. This can be understood by considering the following three figures of merit for the EUV emission from the plasma: CE, spectral purity (SP), and radiative efficiency. As discussed in the Introduction, CE represents the ratio of $E_{ib,2\pi}$ over the energy of the drive laser (E_{laser}). Here, $E_{ib,2\pi}$ is the total in-band radiation emitted into the half-sphere back towards the laser that is covered by light collection optics

$$CE = E_{ib,2\pi}/E_{laser}. \tag{5}$$

SP is the ratio of $E_{ib,2\pi}$ and total EUV energy ($E_{rad,2\pi}$) emitted in the same half-sphere

$$SP = E_{ib,2\pi}/E_{rad,2\pi}. \tag{6}$$

Energy conservation dictates that SP is the absolute upper limit to the conversion efficiency: CE $\leqslant$ SP. A more stringent limit of CE $\leqslant$ SP/2 is obtained for spherically symmetric emission [120]. SP is significantly influenced by the optical depth, and thus, opacity. This influence on SP can be understood by considering the equation for radiative transport, which yields the spectral radiance L_λ. The solution to such radiative transport equations can be given in analytic form for a homogeneous one-dimensional plasma

$$L_\lambda = S_\lambda(1 - e^{-\tau_\lambda}), \tag{7}$$

where $S_\lambda = j_\lambda/\alpha_\lambda$ is the source function with the coefficients for emissivity j_λ and absorptivity α_λ. Opacity is given by $\kappa_\lambda = \alpha_\lambda/n_i$, where n_i is the matter (ion) density. Source function S_λ equals the Planck blackbody function B_λ in thermodynamic equilibrium where the atomic levels are thermally populated. In the exponent, τ_λ is the wavelength-specific optical depth given by $\tau_\lambda = \int \alpha_\lambda dx$ where the absorptivity coefficient α_λ is integrated over the plasma length. In the limiting case $\tau_\lambda \ll 1$ the spectral radiance is given by that of a line emitter $L_\lambda = S_\lambda \tau_\lambda = j_\lambda l$ with length l [10]. In the other extreme, at large optical depths $\tau_\lambda \gg 1$, we find $L_\lambda = S_\lambda = B_\lambda$, a blackbody. Absorptivity α_λ and length scale thus comprise the optical depth and an increase in either term will increase the width of the emission features through equation (7) and with it, decrease SP.

Figure 11 (upper panel) shows the dependence of the spectral efficiency of the plasma emissivity j_λ on plasma ion density and electron temperature. Spectral efficiency equals SP for infinitesimal plasma size. The spectral efficiency is seen to monotonically decrease with the plasma ion density ranging from a 40% value for very low-density plasmas, over a 30% value representative for the CO_2 case to 20% for the Nd:YAG case. Similar results were obtained more recently with more detail at KIAM by Novikov and coworkers [121] who also compared results from partial-LTE to collisional radiative modeling. Significant differences occur especially at
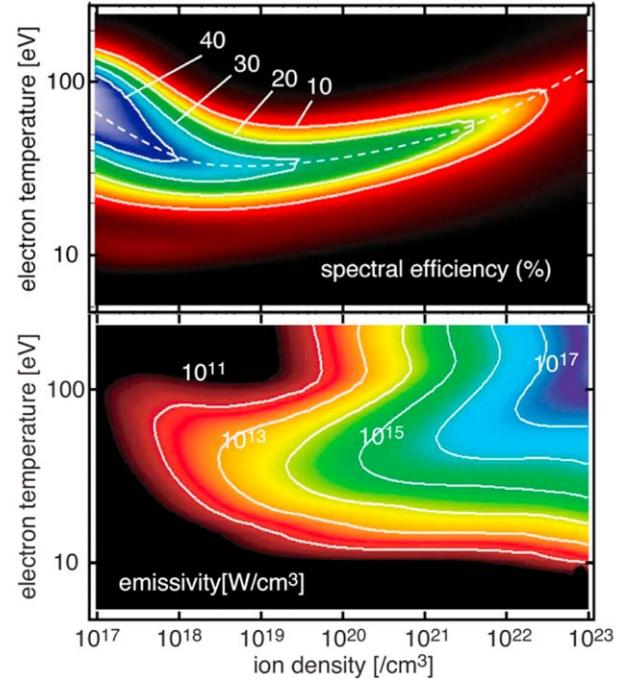

Figure 11. (Upper) calculated isocontour profile of the spectral efficiency of the Sn plasma emissivity j_λ given from 10% to 40% value at 10% increment. Reproduced from [119]. (Lower) emissivity of 13.5 nm radiation from integrated over a 2% bandwidth. Note that the plasma ion and electron density differ by the value of the average charge state ($\bar{Z} \approx 10$). Electron and ion temperatures will be almost equal. Reproduced from [118].

the lower plasma densities. Complete inclusion of complex atomic plasma processes such as dielectronic recombination [122] and electron impact ionization [123] and excitation of the many-electron tin ions is required to move beyond the LTE approximation. However those fundamental data are by and large still lacking.

The plasma emissivity in the 2% bandwidth around 13.5 nm increases with both temperature and density as seen in figure 11 (lower panel). However, the emission from the densest regions cannot escape the plasma because of opacity. Simulation results such as shown in figure 11 feed into hydrodynamics codes with proper accounting of radiation transport enabling finding the optimum plasma conditions in terms of temperature and density.

The third and last figure of merit is the radiative efficiency η_{rad} defined as the ratio of EUV $E_{rad,2\pi}$ to the laser pulse energy E_{laser} and equals the ratio of the first two figures of merit CE/SP

$$\eta_{rad} = E_{rad,2\pi}/E_{laser} = CE/SP. \tag{8}$$

Even though laser absorption is not complete in the CO_2 case, with some 30% of the light reflected backwards in the direction of the laser, the CE of drive laser light into in-band radiation is remarkably high at values surpassing 5.5%. These large CE values are facilitated by the relatively low densities, which lead to a near optimal optical depth [120]: high enough
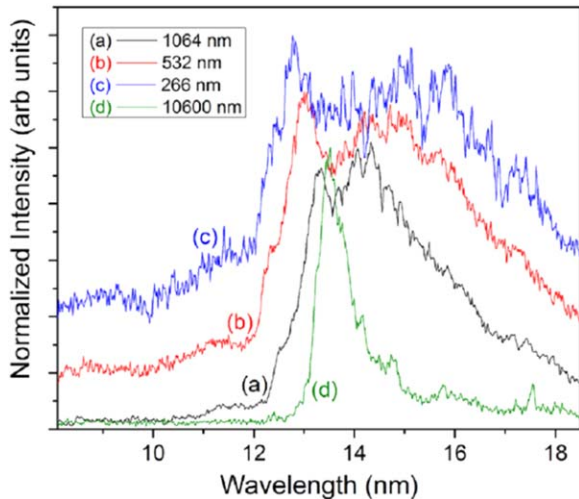
Figure 12. Laser wavelength dependence on the EUV emission from laser-produced Sn plasmas. Shown are normalized EUV emission spectra from LPP driven by the Nd:YAG fundamental, second and fourth harmonic as well as from a 10.6 μm wavelength CO$_2$-laser driven LPP. The second (b) and fourth (c) harmonic spectra are displaced vertically for better visibility. Reproduced from [126].

to provide high emissivity, but low enough to avoid any broadening of the main emission feature [10, 120].

Changing drive laser wavelength to the 1 μm Nd:YAG entails an increase in the critical density by two orders of magnitude. Nearly 100% of the impinging Nd:YAG laser light is absorbed, a significant fraction of it in the underdense region [43]. Simulation works predict that 70%–90% of the absorbed Nd:YAG laser light is emitted as radiation [23, 124, 125]. However, depending on the typical length scales involved, the plasma may be optically thick for its own radiation and in-band emission features could broaden well beyond the bandwidth reflected by the multilayer optics. Further decreasing the wavelength of the drive laser light will lead to even higher-density plasma, which could lead to more broadening [126], as is illustrated in figure 12. In fact, the plasma can become so optically thick that self-absorption dips in the emission spectra show up at the wavelengths of the strong transitions near 13.5 nm with the largest Einstein coefficients. First traces of these dips may already appear in the spectrum of a plasma driven by the fundamental 1 μm wavelength of a Nd:YAG laser system (see figure 12). Several routes may however be identified to prevent such strong opacity effects.

3.3. Routes for optimizing in-band EUV emission

The large increase in industrial source performance over the last few years shown in figure 2 is a result of the maturing of the physical understanding of the complex plasma physics and engineering required to realize such high output powers [11]. Improvements in the main pulse characteristics, in addition to target formation developments, have enabled access to favorable plasma conditions [11, 16, 127, 128], leading to CE values exceeding 5.5% and output powers beyond 250 W. With theory predicting CE to be

fundamentally limited only near 9%, at about half the value of the theoretical maximum of 20% for the hypothetical case of a uniform static Sn plasma [120], further increases in source performance may be expected.

Ongoing developments on industrializing high-power 1 μm wavelength Nd:YAG lasers make them a promising alternative to the CO$_2$-lasers. Such solid-state lasers would offer significant advantages. These advantages include an improved energy efficiency in terms of converting electrical power into optical power, better stability and reliability, and a significantly more compact size at the same output power. Moreover, it would offer more straightforward temporal and spatial pulse shaping capabilities that provide further handles for improving source performance. These lasers may in fact replace CO$_2$ lasers if the efficiency of converting laser energy into in-band radiation is shown to be sufficiently competitive. In this topical review, some key characteristics of the plasmas created by both types of lasers have been discussed and compared. In summary, Nd:YAG-driven light sources have a much higher, near complete laser absorptivity due to the strong increase of the electron density with decreasing wavelength [50]. However, for the same reason they suffer from self-absorption of the emitted EUV light [120, 126, 129]. Available literature on Nd:YAG-laser-produced Sn plasma deals with the emission from planar solid targets [117, 130–140], or tin-coated spherical targets [98, 141–144]. Literature covering the emission properties of the industrially relevant tin microdroplets, driven by a Nd:YAG laser, remains scarce [145–147]. It is therefore an open question what is the fundamental limit value of the CE of such Nd:YAG-driven sources.

Schupp and coworkers [30] performed measurements on such LPPs and determined CE, SP and the corresponding radiative efficiency of the emission of EUV light (see figures 7 and 13). They used a novel broadband transmission-grating spectrometer [148, 149]. The laser intensity was found to be the pertinent parameter setting the plasma temperature and, thus, the tin ion charge state distribution. SP values were found to systematically decrease with increasing tin droplet diameter D_0 or the laser pulse duration τ_p. This finding is in line with expectations from equation (7) as the typical plasma length scale will increase with both D_0 and τ_p. For none of the parameter sets self-absorption dips showed up in contrast to the work by Freeman and coworkers (compare figures 7 and 12). The key difference between the two experiments is the use of droplet targets (in figure 7) versus a solid planar target (figure 12). Droplet targets are thus seen to generally, spectrally outperform solid targets. This better performance may be explained by considering the following two factors. First, the planar target is larger than the laser beam focus and a non-uniform temperature profile will be established that may be detrimental to in-band EUV emission. Second, a very different plasma rarefaction geometry is established: a rarefaction $n \sim R_f^{-\alpha}$ [150] can generally be expected with $\alpha = 3$ for the spherical expansion of the droplet target while for planar expansion a far less advantageous $\alpha = 1$ rarefaction occurs.
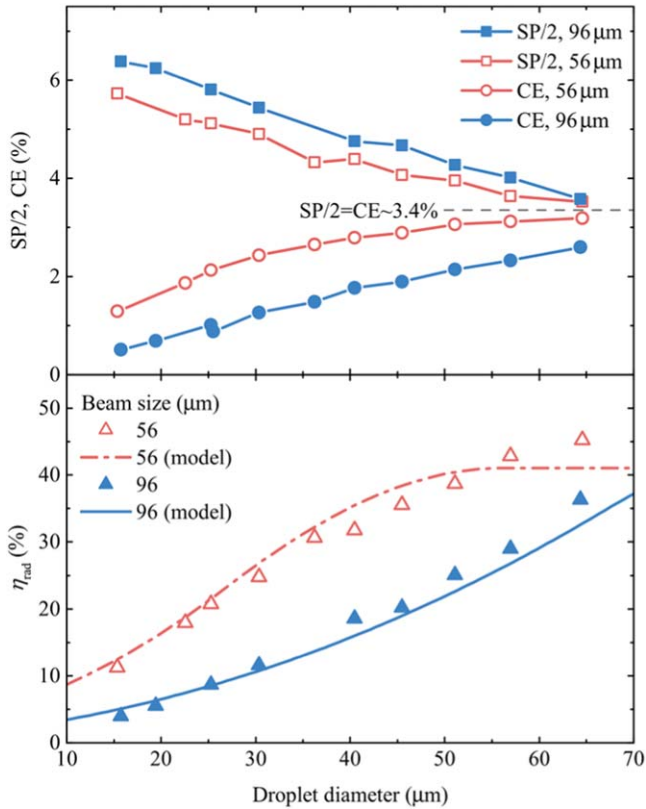
Figure 13. Analysis of spectral data obtained from Nd:YAG-driven tin-droplet plasma at a laser intensity of 1.4×10^{11} W cm^{-2}: (upper) values for spectral purity (SP) and conversion efficiency (CE) versus droplet diameter for two different laser beam sizes (56 and 96 μm as indicated in the legend); (lower) corresponding radiative efficiencies versus droplet diameter. The lines represent model estimates, see text. Reproduced from [30].

Figure 13 also shows a monotonically increasing CE with increasing tin droplet diameter or laser pulse duration. This behavior can be linked to the radiative efficiency equation (8). The dependencies of the radiative efficiency on the experimental parameters can be successfully captured in a model that features the plasma absorption length as the primary parameter [30]. This understanding enables the optimization of both η_{rad} and SP, finding a global optimum of the conversion efficiency CE = η_{rad}SP. A record-high 3.2% CE was obtained and further paths were identified for improving this efficiency, capitalizing on the ongoing development of advanced YAG laser systems [34, 151]. YAG lasers may also find application in two-color pumping schemes. In such novel schemes, a low-intensity short-wavelength (Nd:YAG) pulse may be used to control the rate of mass ablation while a high-intensity long-wavelength CO_2 pulse provides efficient generation of in-band EUV light [120].

Considering the trade-off between absorptivity and opacity, a globally optimum performance of plasma EUV light sources may in fact be found for drive laser wavelengths in between the Nd:YAG and CO_2 cases of 1 and 10 μm, respectively. New possible drive laser architectures include the 1.9 μm wavelength, high-efficiency big aperture thulium laser that uses Tm:YLF as a laser medium [152]. Such

scalable diode-pumped solid state lasers share several of the advantages of the common Nd:YAG and could well drive the next generation of EUV sources. Preliminary investigations using one-dimensional simulations using LLNL's HYDRA code [153] evidence conversion efficiencies that may equal or even exceed those of the CO_2-driven plasma [152]. Experimental work is required to validate such exciting predictions.

Most experimental work is performed at low 10 Hz repetition rates. Scaling this rate up by three or even four orders of magnitude to meet the industrial demand for output power is non-trivial [154, 155]. Under such industrial conditions a steady-state plasma is created that influences the buffer gas flow (see section 4). The pulsed plasma furthermore impacts on the droplet that is next in line and can significantly deform it into a shape that is no longer amenable to optimum target formation through prepulse interactions. Nevertheless, the recent low-repetition rate investigations open up a new exiting avenue of scientific exploration to understand and further control the limiting effects of opacity of dense plasma.

4. Plasma expansion: ion kinetic energy distributions

Besides the wanted EUV light, LPP produces debris that may limit the lifetime of the light collecting multilayer optics. This debris can comprise tin droplet fragments, neutral atoms or clusters, and plasma ions. Under optimal operating conditions, full evaporation of the target material is achieved and only plasma ions and atoms are produced, expanding into the vacuum. Such plasma expansion is a subject of particular interest for a broad range of applications ranging from ultracold plasmas [156, 157] over laser acceleration [158, 159] to EUV and even shorter wavelength light sources [9–11]. The plasma ions with mass m can obtain significant kinetic energy, of the order of several times the speed of sound c_s in the corona [43]

$$c_s \sim \sqrt{Zk_B T/m} \sim (5-10) \times 10^3\, T^{1/2}, \qquad (9)$$

in units of m/s with T entered in eV. The energetic particles can damage the collector through sputtering or implantation. The industry mitigates debris through the use of a hydrogen buffer gas. The choice of element, H_2, has two key benefits. Atomic hydrogen, produced from the molecules under the influence of the plasma, reacts with any deposited tin to form ultimately the gaseous stannane (SnH_4) that can be pumped out of the source vessel. Further, of all gases H_2 has the lowest EUV absorption cross section but still sufficient stopping power. Another approach, a magnetic guidance technique has shown benefits by redirecting tin ions away from the collector mirror (see figure 1). However, this solution requires large magnetic fields and a hydrogen flow is still needed for debris mitigation [58]. Detailed scientific studies of this alternative have yet to enter the public literature. The pressure of the buffer gas determines its Sn-ion stopping power. Stopping power is a function of the kinetic energy of the Sn ion [160]. Understanding Sn–H_2 collisions on the

fundamental level is key to set the optimal pressure. If the ions are not mitigated they will interact, among others, with the multilayer optics. This interaction between projectile atoms and surfaces can be simulated to predict the consequences. The most commonly used simulation package is SRIM [161], which however shows notable discrepancies with the available experimental data at the relevant, relatively low impact energies. Thus, detailed Sn-metal collision studies also need to be performed. An essential input for such collision studies is the charge and energy distribution of the ions.

Charge and energy distributions measured for different pulse durations of a Nd:YAG laser on both solid-planar and liquid-droplet targets have been measured by several groups [33, 100, 126, 162–166]. In most cases, Faraday cups (FCs) were used that yield charge-averaged energy spectra from the obtained time-of-flight traces of the measured currents. FCs are robust and compact diagnostic tools that can also readily be used to characterize the angular distribution of ion emission by mounting them under different angles.

LPPs can be created over a large space of laser and target parameters. Bayerle and coworkers addressed the energy distributions of emitted ions in a substantial subset of this space for both 1 μm wavelength prepulses and main pulses [35]. Pulse lengths ranged from ps to ns and laser peak fluences reached up to 3 kJ cm^{-2}. Plasma was produced from both solid-planar and liquid-droplet targets. The authors compared their charge-averaged results to two well-known analytical solutions of single-fluid (and single-charge-state) hydrodynamics models of plasma expansion into vacuum [150, 167] (also see [168, 169]). In the hydrodynamic approach the expanding plasma is assumed to be a quasi-neutral fluid, and the energy spectrum of the ions is identified with the asymptotic (at $t \to \infty$) energy spectrum. They found that the self-similar solution to a semi-infinite planar plasma expanding isothermally with an initial exponential density profile, shows remarkably good agreement with the experimental results of the LPP produced by ps-laser pulses, as illustrated in figure 14. The model [167, 168] describes the particle energy distribution dN/dE for a characteristic energy E_0 through

$$\mathrm{d}N/\mathrm{d}E \propto (E/E_0)^{-1/2} \exp(-\sqrt{E/E_0}). \qquad (10)$$

Ion energy distributions obtained by exposing solid Sn targets to ns-laser pulses at relatively low fluence agree best with the solution to a different hydrodynamics model [150], with a distribution given by

$$\mathrm{d}N/\mathrm{d}E \propto (E/E_0)^{(\alpha-2)/2} \exp(-E/E_0), \qquad (11)$$

with a slightly different definition of the characteristic energy E_0. Now, the (again isothermal) plasma density evolution starts out from a Gaussian density profile [170, 171] and the model takes into account the dimensionality α of the plasma expansion. The comparisons between theory and experiment as shown in figure 14 did not aim to reach the accuracy level that may be required to pinpoint physics related the possible presence of a double layer [167, 172, 173] or a non-Maxwellian distribution of the electrons [174, 175]. Nevertheless, the work of Bayerle and coworkers [35], and several others
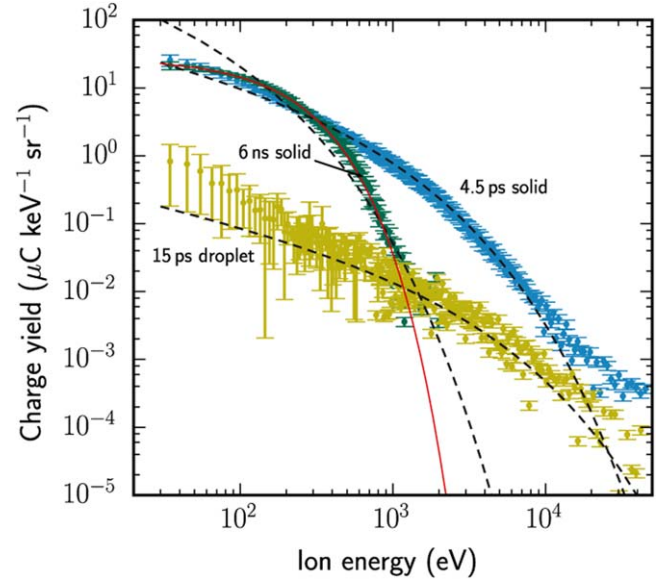

Figure 14. Charge and energy distributions measured with Faraday cups for different pulse durations of a Nd:YAG laser on both solid-planar and liquid-droplet targets. The energy density of the laser pulses is approximately 25 J cm^{-2}. The dashed (black) lines show the fits of the single-fluid (single-charge-state) exponential-density-profile model equation (10) to the distributions. The solid (red) line is a fit of the Gaussian-density-profile model equation (11) to the data (with cylindrical dimensionality $\alpha = 2$). Reproduced from [35].

[150, 176, 177] show that relatively simple models are apparently sufficient to explain the gross features of the measured charge-state-averaged ion energy distributions.

Tailoring plasma profiles can be beneficial for source operation by enabling a measure of control of the ion kinetic energy distributions. Notable examples are the use of double laser pulses [178], and more specifically the recent use of picosecond pulse pairs as a prepulse [34].

A complete description of the plasma expansion however requires charge-state-resolved kinetic energy spectra [98, 172, 179, 180]. Such information would enable, for instance, to determine the energy or momentum imparted on the buffer gas [11] flowing around the LPP. Charge-energy spectra can be obtained by employing, e.g. retarding-field Faraday cups (RFA) [181–184], electrostatic analyzers (ESA) [32, 115, 185], or Thomson parabola (TP) [98, 186, 187]. Each detector type has been used in the past to diagnose tin LPPs [32, 98, 183, 185]. TPs stand out as they allow for measuring charge-energy spectra for a single laser shot. ESA measurements of ns-pulse driven plasma show that high charge states beyond 6+ contribute to the spectra of both Nd:YAG (for example, see figure 15) and CO_2 driven tin plasma. The accuracy of ESA measurements such as shown in figure 15 can be gauged by comparing the charge-weighted sum-over-charges (black line) to those obtained from the summed-charge-state FC (red line). Excellent agreement between the two methods is obtained in this case. Calibration of the, e.g. channeltron or microchannel plate detector response function is of key importance [188, 189].

In general terms, shorter wavelength-driven sources are associated with higher recombination rates [115], and thus,

lower average charge state, but higher overall kinetic energies. The understanding of the charge-energy spectrum however is far from complete. New theoretical insights are required, beyond the single charge state approximations, bench-marked by more detailed experimental campaigns. Such joint insights from theory and experiment may enable further control of the kinetic energy spectrum of the ions originating from the expanding plasma, benefiting the lifetime of the optics housed in the source module and relaxing design constraints originating from the various mitigation techniques.

5. Conclusions

In this topical review, key physics aspects of laser-produced transient tin plasmas are discussed. These plasmas are the sources of EUV light at 13.5 nm wavelength for next-generation EUV nanolithography. They will enable driving Moore's law well into the future. Generating ever more EUV light provides a formidable and continuing multi-faceted task. Physical processes span more than six orders of magnitude in time, ranging from the ps and ns time scales of the laser-driven plasma processes to the μs scale on which the tin target deforms by the fluid dynamics started by the laser impact. The impressive increase in industrial source performance over the last few years results from advancement of the physical understanding of the atomic plasma processes and the engineering required to realize high output powers. Such advances enabled CE values exceeding 5.5% and output powers beyond 250 W, leading to the adoption of EUV nanolithography in high-volume manufacturing. Further progress is to be expected not only in CO_2-gas-laser driven systems, but also from solid-state laser-driven plasma sources. Progress in this field was, is, and will continue to be achieved by strong interaction and collaborations between fundamental research and industrial innovations.
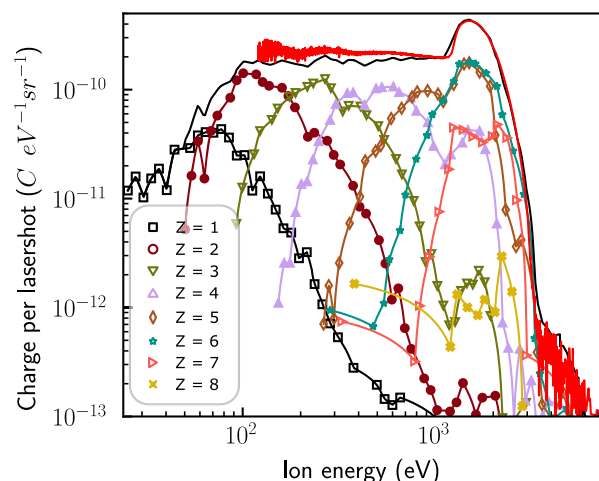
Acknowledgments

Figure 15. Charge energy distributions measured from a droplet plasma at a 10 ns pulse Nd:YAG laser energy of 75 mJ. The red solid line is obtained from a Faraday cup. The black solid line is the results of summing the individual charge energy distributions as obtained from an electrostatic analyzer.

ORCID iDs

Oscar O Versolato https://orcid.org/0000-0003-3852-5227

References

[1] Moore G E 1965 *Electronic* **38** 114–7
[2] Moore G E 1975 *Proc. IEDM Tech. Dig.* **11** 11–3
[3] Mack C A 2011 *IEEE Trans. Semicond. Manuf.* **24** 202
[4] Waldrop M M 2016 *Nature* **530** 144
[5] Moore G E 1995 *Proc. SPIE* **2439**
[6] van Schoot J *et al* 2018 *Proc. SPIE* 10583
[7] Bajt S, Alameda J B, Barbee T W Jr, Clift W M, Folta J A, Kaufmann B and Spiller E A 2002 *Opt. Eng.* **41** 1797
[8] Huang Q, Medvedev V, van de Kruijs R, Yakshin A, Louis E and Bijkerk F 2017 *Appl. Phys. Rev.* **4** 011104
[9] Banine V Y, Koshelev K N and Swinkels G H P M 2011 *J. Phys. D: Appl. Phys.* **44** 253001
[10] Bakshi V (ed) 2006 *EUV Sources for Lithography* (Bellingham, WA: SPIE Press)
[11] Bakshi V (ed) 2018 *EUV Lithography* 2nd edn (Bellingham, WA: SPIE Press)
[12] Bauche J, Bauche-Arnoult C and Peyrusse O 2015 *Atomic Properties in Hot Plasmas* (New York: Springer International Publishing)
[13] O'Sullivan G *et al* 2015 *J. Phys. B: At. Mol. Opt. Phys.* **48** 144025
[14] Colgan J, Kilcrease D, Abdallah J, Sherrill M, Fontes C, Hakel P and Armstrong G 2017 *High Energy Density Phys.* **23** 133
[15] Purvis M *et al* 2018 *Proc. SPIE* **10583** 10583
[16] Fomenkov I *et al* 2017 *Adv. Opt. Technol.* **6** 173
[17] Lercel M 2019 private communication

[18] Kurilovich D, Klein A L, Torretti F, Lassise A, Hoekstra R, Ubachs W, Gelderblom H and Versolato O O 2016a *Phys. Rev. Appl.* **6** 014018

[19] Hudgins D, Gambino N, Rollinger B and Abhari R 2016 *J. Phys. D: Appl. Phys.* **49** 185205

[20] Klein A L, Bouwhuis W, Visser C W, Lhuissier H, Sun C, Snoeijer J H, Villermaux E, Lohse D and Gelderblom H 2015 *Phys. Rev. Appl.* **3** 044018

[21] Kurilovich D, Klein A L, Torretti F, Lassise A, Hoekstra R, Ubachs W, Gelderblom H and Versolato O O 2016b *Phys. Rev. Appl.* **6** 014018

[22] Gelderblom H, Lhuissier H, Klein A L, Bouwhuis W, Lohse D, Villermaux E and Snoeijer J H 2016 *J. Fluid Mech.* **794** 676

[23] Kurilovich D, Basko M M, Kim D A, Torretti F, Schupp R, Visschers J C, Scheers J, Hoekstra R, Ubachs W and Versolato O O 2018 *Phys. Plasmas* **25** 012709

[24] Vinokhodov A, Krivokorytov M, Sidelnikov Y, Krivtsun V, Medvedev V, Bushuev V, Koshelev K, Glushkov D and Ellwi S 2016a *Rev. Sci. Instrum.* **87** 103304

[25] Basko M M, Krivokorytov M S, Vinokhodov A Y, Sidelnikov Y V, Krivtsun V M, Medvedev V V, Kim D A, Kompanets V O, Lash A A and Koshelev K N 2017 *Laser Phys. Lett.* **14** 036001

[26] Krivokorytov M S, Vinokhodov A Y, Sidelnikov Y V, Krivtsun V M, Kompanets V O, Lash A A, Koshelev K N and Medvedev V V 2017 *Phys. Rev.* E **95** 031101

[27] Kurilovich D *et al* 2018 *Phys. Rev. Appl.* **10** 054005

[28] Grigoryev S Y *et al* 2018 *Phys. Rev. Appl.* **10** 064009

[29] Koukouvinis P, Kyriazis N and Gavaises M 2018 *PLoS One* **13** 1

[30] Schupp R *et al* 2019 *Phys. Rev. Appl.* **12** 014010

[31] Benschop J, Banine V, Lok S and Loopstra E 2008 *J. Vac. Sci. Technol.* B **26** 2204

[32] Giovannini A Z, Gambino N, Rollinger B and Abhari R S 2015 *J. Appl. Phys.* **117** 033302

[33] Deuzeman M J *et al* 2017 *J. Appl. Phys.* **121** 103301

[34] Stodolna A S, de Faria Pinto T, Ali F, Bayerle A, Kurilovich D, Mathijssen J, Hoekstra R, Versolato O O, Eikema K S E and Witte S 2018 *J. Appl. Phys.* **124** 053303

[35] Bayerle A *et al* 2018 *Plasma Sources Sci. Technol.* **27** 045001

[36] Fujioka S *et al* 2008 *Appl. Phys. Lett.* **92** 241502

[37] Mizoguchi H *et al* 2010 *Proc. SPIE* **7636** 763608

[38] Phipps C R *et al* 1988 *J. Appl. Phys.* **64** 1083

[39] Fabbro R, Max C and Fabre E 1985 *Phys. Fluids* **28** 1463

[40] Hassanein A, Sizyuk T, Sizyuk V A and Harilal S S 2011 *J. Micro Nanolithogr. MEMS MOEMS* **10** 033002

[41] Freeman J, Harilal S and Hassanein A 2011 *J. Appl. Phys.* **110** 083303

[42] Freeman J, Harilal S, Hassanein A and Rice B 2013 *Appl. Phys.* A **110** 853

[43] Basko M M, Novikov V G and Grushin A S 2015 *Phys. Plasmas* **22** 053111

[44] Tsygvintsev I P, Krukovskiy A Y and Novikov V G 2014 *2014 Int. Workshop on EUV and Soft X-Ray Sources*

[45] Reijers S A, Kurilovich D, Torretti F, Gelderblom H and Versolato O O 2018 *J. Appl. Phys.* **124** 013102

[46] Kidder R 1968 *Nucl. Fusion* **8** 3

[47] Afanas'ev Y V and Krokhin O N 1972 Gas-dynamical theory of the effect of laser radiation on condensed substances *Quantum Electronics in Lasers and Masers: Part 2* ed D V Skobel'tsyn (Boston, MA: Springer) pp 109–55

[48] Afanas'ev Y V, Gamalii E G, Krokhin O N and Rozanov V B 1976 *Sov. Phys.—JETP* **44** 311

[49] Manheimer W M, Colombant D G and Gardner J H 1982 *Phys. Fluids* **25** 1644

[50] Mora P 1982 *Phys. Fluids* **25** 1051

[51] Atzeni S and Meyer-ter Vehn J 2004 *The Physics of Inertial Fusion: BeamPlasma Interaction, Hydrodynamics, Hot Dense Matter* (Oxford: Oxford University Press)

[52] Mulser P and Bauer D 2010 *High Power Laser-Matter Interaction* (*Springer Tracts in Modern Physics*) vol 238 (Berlin: Springer)

[53] Zhou L, Li X-Y, Zhu W-J, Wang J-X and Tang C-J 2015 *J. Appl. Phys.* **117** 125904

[54] Chichkov B N, Momma C, Nolte S, von Alvensleben F and Tuennnermann A 1996 *Appl. Phys.* A **63** 109

[55] Gamaly E G, Rode A V, Luther-Davies B and Tikhonchuk V T 2002 *Phys. Plasmas* **9** 949

[56] Masnavi M, Nakajima M, Horioka K, Araghy H P and Endo A 2011 *J. Appl. Phys.* **109** 123306

[57] Lakatosh B V, Abramenko D B, Ivanov V V, Medvedev V V, Krivtsun V M, Koshelev K N and Yakunin A M 2018 *Laser Phys. Lett.* **15** 016003

[58] Kawasuji Y *et al* 2017 *Proc. SPIE* **10143** 101432G

[59] Thoroddsen S T, Takehara K, Etoh T and Ohl C-D 2009 *Phys. Fluids* **21** 112101

[60] Gonzalez-Avila S R, Klaseboer E, Khoo B C and Ohl C-D 2011 *J. Fluid Mech.* **682** 241

[61] Krivokorytov M S, Zeng Q, Lakatosh B V, Vinokhodov A Y, Sidelnikov Y V, Kompanets V O, Krivtsun V M, Koshelev K N, Ohl C-D and Medvedev V V 2018 *Sci. Rep.* **8** 597

[62] Villermaux E 2007 *Annu. Rev. Fluid Mech.* **39** 419

[63] Basko M M, Maruhn J A and Tauschwitz A 2009 *J. Comput. Phys.* **228** 2175

[64] Basko M M, Maruhn J A and Tauschwitz A 2010 Development of a 2D radiation-hydrodynamics code RALEF for laser plasma simulations *GSI Report* 2010–1, PLASMA-PHYSICS-25 GSI Helmholtzzentrum für Schwerionenforschung GmbH

[65] Sokolowski-Tinten K, Bialkowski J, Cavalleri A, von der Linde D, Oparin A, Meyer-ter-Vehn J and Anisimov S I 1998 *Phys. Rev. Lett.* **81** 224

[66] von der Linde D and Sokolowski-Tinten K 2000 *Appl. Surf. Sci.* **154-155** 1

[67] Vledouts A, Quinard J, Vandenberghe N and Villermaux E 2016 *J. Fluid Mech.* **788** 246

[68] Uylings P, Raassen A and Wyart J-F 1993 *J. Phys. B: At. Mol. Opt. Phys.* **26** 4683

[69] Hansen J, Uylings P and Raassen A 1988 *Phys. Scr.* **37** 664

[70] Cowan R D 1981 *The Theory of Atomic Structure and Spectra* (Berkeley, CA: University of California Press)

[71] Bauche J, Bauche-Arnoult C and Klapisch M 1988 *Adv. Atom. Mol. Phys.* **23** 131

[72] Bauche-Arnoult C, Bauche J and Klapisch M 1984 *Phys. Rev.* A **30** 3026

[73] Windberger A *et al* 2015 *Phys. Rev. Lett.* **114** 150801

[74] Azarov V I and Joshi Y N 1993 *J. Phys. B: At. Mol. Opt. Phys.* **26** 3495

[75] Svendsen W and O'Sullivan G 1994 *Phys. Rev.* A **50** 3710

[76] Churilov S S and Ryabtsev A N 2006a *Phys. Scr.* **73** 614

[77] Churilov S S and Ryabtsev A N 2006b *Opt. Spectrosc.* **100** 660

[78] Churilov S S and Ryabtsev A N 2006c *Opt. Spectrosc.* **101** 169

[79] Ryabtsev A N, Kononov É Y and Churilov S S 2008 *Opt. Spectrosc.* **105** 844

[80] Tolstikhina I Y, Churilov S S, Ryabtsev A N and Koshelev K N 2006 *EUV Sources for Lithography* ed V Bakshi (Bellingham, WA: SPIE Press) ch 4 pp 113–48

[81] D'Arcy R *et al* 2009 *Phys. Rev.* A **79** 042509

[82] Ohashi H, Suda S, Tanuma H, Fujioka S, Nishimura H, Sasaki A and Nishihara K 2010 *J. Phys. B: At. Mol. Opt. Phys.* **43** 065204

[83] Windberger A *et al* 2016 *Phys. Rev.* A **94** 012506

[84] Torretti F *et al* 2017 *Phys. Rev.* A **95** 042503
[85] Epp S W *et al* 2010 *J. Phys. B: At. Mol. Opt. Phys.* **43** 194008
[86] Torretti F, Schupp R, Kurilovich D, Bayerle A, Scheers J, Ubachs W, Hoekstra R and Versolato O 2018 *J. Phys. B: At. Mol. Opt. Phys.* **51** 045005
[87] Morris O, Hayden P, O'Reilly F, Murphy N, Dunne P and Bakshi V 2007 *Appl. Phys. Lett.* **91** 081506
[88] Sakaguchi H *et al* 2008 *Appl. Phys. Lett.* **92** 111503
[89] Gambino N, Rollinger B, Brandstätter M and Abhari R S 2016 *Spectrochim. Acta* B **122** 149
[90] Davydova N *et al* 2015 *31st European Mask and Lithography Conf.* 9661 (Bellingham, WA: SPIE Press) p 96610B
[91] Purvis M A *et al* 2016 *Extreme Ultraviolet (EUV) Lithography VII* 9776 (Bellingham, WA: SPIE Press) p 97760K
[92] Sizyuk V, Hassanein A, Morozov V, Tolkach V, Sizyuk T and Rice B 2006 *Numer. Heat Transfer* A **49** 215
[93] Sizyuk V, Sizyuk T, Hassanein A and Johnson K 2018 *J. Appl. Phys.* **123** 013302
[94] Koshelev K, Ivanov V V, Medvedev V, Krivtsun V M, Novikov V G and Grushin A S 2012 *J. Micro Nanolithogr. MEMS MOEMS* **11** 029802
[95] Basko M M, Novikov V G and Grushin A S 2014 *2014 Int. Workshop on EUV and Soft X-Ray Sources (Dublin, November 3–6)* http://euvlitho.com/2014/S36.pdf
[96] Fontes C, Zhang H, Abdallah J Jr, Clark R, Kilcrease D, Colgan J, Cunningham R, Hakel P, Magee N and Sherrill M 2015 *J. Phys. B: At. Mol. Opt. Phys.* **48** 144014
[97] Hakel P, Sherrill M, Mazevet S, Abdallah J Jr, Colgan J, Kilcrease D, Magee N, Fontes C and Zhang H 2006 *J. Quant. Spectrosc. Radiat. Transfer* **99** 265
[98] Fujioka S *et al* 2005 *Appl. Phys. Lett.* **87** 241503
[99] Roy A, Harilal S S, Hassan S M, Endo A, Mocek T and Hassanein A 2015 *Laser Part. Beams* **33** 175
[100] Coons R W, Harilal S S, Campos D and Hassanein A 2010 *J. Appl. Phys.* **108** 1
[101] Harilal S S, O'Shay B, Tillack M S and Mathew M V 2005 *J. Appl. Phys.* **98** 013306
[102] Lan H, Lei H, Zuo D, Wang X and Zheng G 2017 *Vacuum* **135** 86
[103] Iqbal J, Ahmed R, Rafique M, Anwar-ul Haq M and Baig M A 2016 *Laser Phys.* **26** 076001
[104] Namba S *et al* 2008 *J. Appl. Phys.* **104** 013305
[105] Kieft E R, van der Mullen J J A M, Kroesen G M W, Banine V and Koshelev K N 2004 *Phys. Rev.* E **70** 066402
[106] Scheers J *et al* 2018 *Phys. Rev.* A **98** 062503
[107] Tomita K *et al* 2017 *Sci. Rep.* **7** 12328
[108] Tomita K *et al* 2015 *Appl. Phys. Express* **8** 126101
[109] Brunel F 1987 *Phys. Rev. Lett.* **59** 52
[110] Yakunin A M, Ivanov V V, Krivtsun V M, Medvedev V, Swinkels G H P M and Van Schoot J B P 2016 Radiation source *US Patent* 9,366,967
[111] Johnston T W and Dawson J M 1973 *Phys. Fluids* **16** 722
[112] Nemchinov I V 1967 *J. Appl. Math. Mech.* **31** 320
[113] Basov N G, Gribkov V A, Krokhin O N and Sklizkov G V 1968 *Sov. Phys.—JETP* **27** 575
[114] Harilal S S, Sizyuk T, Hassanein A, Campos D, Hough P and Sizyuk V 2011 *J. Appl. Phys.* **109** 063306
[115] Burdt R A, Yuspeh S, Sequoia K L, Tao Y, Tillack M S and Najmabadi F 2009 *J. Appl. Phys.* **106** 033310
[116] Colombant D and Tonon G 1973 *J. Appl. Phys.* **44** 3524
[117] White J, Dunne P, Hayden P, O'Reilly F and O'Sullivan G 2007 *Appl. Phys. Lett.* **90** 181502
[118] Nishihara K *et al* 2008a *Phys. Plasmas* **15** 056708
[119] Nishihara K *et al* 2008 *Emerging Lithographic Technologies XII* vol 6921 (Bellingham, WA: SPIE Press) p 69210Y
[120] Basko M M 2016a *Phys. Plasmas* **23** 083114
[121] Basko M 2016 *2016 Int. Workshop on EUV and Soft X-Ray Sources* https://euvlitho.com/2016/S22.pdf

[122] Badnell N, Foster A, Griffin D, Kilbane D, O'Mullane M and Summers H 2011 *J. Phys. D: Appl. Phys.* **44** 135201
[123] Borovik A Jr, Gharaibeh M F, Hillenbrand P M, Schippers S and Müller A 2013 *J. Phys. B: At. Mol. Opt. Phys.* **46** 175201
[124] O'Shay B, Najmabadi F, Harilal S and Tillack M 2007 *J. Phys.: Conf. Ser.* **59** 773
[125] Tillack M, Sequoia K and Tao Y 2008 *J. Phys.: Conf. Ser.* **112** 042060
[126] Freeman J, Harilal S, Verhoff B, Hassanein A and Rice B 2012a *Plasma Sources Sci. and Technol.* **21** 055003
[127] Fomenkov I 2017 *2017 Int. Workshop on EUV and Soft X-Ray Sources* https://euvlitho.com/2017/S1.pdf
[128] Fomenkov I 2018 *2018 Int. Workshop on EUV and Soft X-Ray Sources* https://euvlitho.com/2018/S1.pdf
[129] Aota T and Tomie T 2005 *Phys. Rev. Lett.* **94** 015004
[130] Spitzer R C, Orzechowski T J, Phillion D W, Kauffman R L and Cerjan C 1996 *J. Appl. Phys.* **79** 2251
[131] Hayden P, Cummings A, Murphy N, O'Sullivan G, Sheridan P, White J and Dunne P 2006 *J. Appl. Phys.* **99** 093302
[132] Ando T *et al* 2006 *Appl. Phys. Lett.* **89** 151501
[133] Tao Y, Harilal S, Tillack M, Sequoia K, O'Shay B and Najmabadi F 2006 *Opt. Lett.* **31** 2492
[134] George S A, Silfvast W T, Takenoshita K, Bernath R T, Koay C-S, Shimkaveg G and Richardson M C 2007 *Opt. Lett.* **32** 997
[135] Morris O, O'Reilly F, Dunne P and Hayden P 2008 *Appl. Phys. Lett.* **92** 2006
[136] Sequoia K L 2009 UC San Diego electronic theses and dissertations *PhD Thesis* UC San Diego
[137] Tao Y, Ueno Y, Yuspeh S, Burdt R, Tillack M and Najmabadi F 2011 *Extreme Ultraviolet (EUV) Lithography II* vol 7969 (Bellingham, WA: SPIE Press) p 796930
[138] Roy A, Murtaza Hassan S, Harilal S S, Endo A, Mocek T and Hassanein A 2014a *Phys. Plasmas* **21** 0
[139] Roy A *et al* 2014b *Appl. Phys. Lett* **105** 074103
[140] Su M, Min Q, Cao S, Sun D, Hayden P, O'Sullivan G and Dong C 2017 *Sci. Rep.* **7** 45212
[141] Shimada Y *et al* 2005 *Appl. Phys. Lett.* **86** 051501
[142] Yuspeh S, Sequoia K, Tao Y, Tillack M, Burdt R and Najmabadi F 2008 *Appl. Phys. Lett.* **93** 221503
[143] Yuspeh S, Tao Y, Burdt R, Tillack M, Ueno Y and Najmabadi F 2011 *Appl. Phys. Lett.* **98** 201501
[144] Freeman J R, Harilal S S, Verhoff B, Hassanein A and Rice B 2012b *Plasma Sources Sci. Technol.* **21** 055003
[145] Giovannini A Z and Abhari R S 2013 *J. Appl. Phys.* **114** 033303
[146] Giovannini A Z 2014 Droplet-based laser-produced plasma sources *PhD Thesis* ETH Zurich, Zurich, Switzerland
[147] Chen H, Wang X, Duan L, Lan H, Chen Z, Zuo D and Lu P 2015 *J. Appl. Phys.* **117** 193302
[148] Goh S, Bastiaens H, Vratzov B, Huang Q, Bijkerk F and Boller K 2015 *Opt. Express* **23** 4421
[149] Bayraktar M, Bastiaens H M, Bruineman C, Vratzov B and Bijkerk F 2016 *NEVAC Blad* **54** 14
[150] Murakami M, Kang Y, Nishihara K, Fujioka S and Nishimura H 2005 *Phys. Plasmas* **12** 062706
[151] Meijer R A, Stodolna A S, Eikema K S E and Witte S 2017 *Opt. Lett.* **42** 2758
[152] Siders C W 2018 *2018 Int. Workshop on EUV and Soft X-Ray Sources* https://euvlitho.com/2018/S15.pdf
[153] Langer S H, Karlin I and Marinak M M 2014 *Int. Conf. on High Performance Computing for Computational Science* (Berlin: Springer) pp 173–81
[154] Sizyuk T and Hassanein A 2015 *Phys. Plasmas* **22** 093101
[155] Vinokhodov A Y, Krivokorytov M S, Sidelnikov Y V, Krivtsun V M, Medvedev V V and Koshelev K N 2016b *J. Appl. Phys.* **120** 163304

[156] Cummings E A, Daily J E, Durfee D S and Bergeson S D 2005 *Phys. Plasmas* **12** 123501

[157] Killian T C, Kulin S, Bergeson S D, Orozco L A, Orzel C and Rolston S L 1999 *Phys. Rev. Lett.* **83** 4776

[158] Flacco A, Guemnie-Tafo A, Nuter R, Veltcheva M, Batani D, Lefebvre E and Malka V 2008 *J. Appl. Phys.* **104** 103304

[159] McKenna P *et al* 2008 *Laser Part. Beams* **26** 591

[160] Abramenko D, Spiridonov M, Krainov P, Krivtsun V, Astakhov D, Medvedev V, van Kampen M, Smeets D and Koshelev K 2018 *Appl. Phys. Lett.* **112** 164102

[161] Ziegler J F, Ziegler M and Biersack J 2010 *19th Int. Conf. on Ion Beam Analysis; Nucl. Instrum. Methods Phys. Res.* B **268** 1818

[162] Thestrup B, Toftmann B, Schou J, Doggett B and Lunney J 2003 *Appl. Surf. Sci.* **208-209** 33

[163] Toftmann B, Doggett B, Budtz-Jørgensen C, Schou J and Lunney J G 2013 *J. Appl. Phys.* **113** 083304

[164] Verhoff B, Harilal S and Hassanein A 2012 *J. Appl. Phys.* **111** 123304

[165] Farid N, Harilal S S, Ding H and Hassanein A 2013 *Phys. Plasmas* **20** 073114

[166] Chen Z, Wang X, Zuo D and Wang J 2016 *Laser Part. Beams* **34** 552

[167] Mora P 2003 *Phys. Rev. Lett.* **90** 185002

[168] Gurevich A V, Pariĭskaya L V and Pitaevskiĭ L P 1966 *J. Exp. Theor. Phys.* **22** 647

[169] Anisimov S I, Bäuerle D and Luk'yanchuk B S 1993 *Phys. Rev.* B **48** 12076

[170] London R and Rosen M 1986 *Phys. Fluids* **29** 3813

[171] Robicheaux F and Hanson J D 2003 *Phys. Plasmas* **10** 2217

[172] Bulgakova N M, Bulgakov A V and Bobrenok O F 2000 *Phys. Rev.* E **62** 5624

[173] Murakami M, Fujioka S, Nishimura H, Ando T, Ueda N, Shimada Y and Yamaura M 2006 *Phys. Plasmas* **13** 033107

[174] Arefiev A V and Breizman B N 2009 *Phys. Plasmas* **16** 055707

[175] Bennaceur-Doumaz D, Bara D and Djebli M 2015 *Laser Part. Beams* **33** 723

[176] Doggett B and Lunney J 2011 *J. Appl. Phys.* **109** 093304

[177] Tanaka N, Masuda M, Deguchi R, Murakami M, Sunahara A, Fujioka S, Yogo A and Nishimura H 2015 *Appl. Phys. Lett.* **107** 114101

[178] Tao Y, Tillack M S, Harilal S S, Sequoia K L and Najmabadi F 2007 *J. Appl. Phys.* **101** 023305

[179] Thum-Jäger A and Rohr K 1999 *J. Phys. D: Appl. Phys.* **32** 2827

[180] Apiñaniz J I, Peralta Conde A and Martinez Perez de Mendiola R 2015 *Eur. Phys. J.* D **69** 265

[181] Dinger R, Rohr K and Weber H 1980 *J. Phys. B: At. Mol. Opt. Phys.* **13** 2301

[182] Demtroder W and Jantz W 1970 *Plasma Phys.* **12** 691

[183] Fomenkov I V *et al* 2009 *Alternative Lithographic Technologies* vol 7271 (International Society for Optics and Photonics) p 727138

[184] Yeates P, Fallon C, Kennedy E T and Costello J T 2011 *Phys. Plasmas* **18** 103104

[185] Rollinger B, Gambino N, Hudgins D, Sanders A, Brandstätter M, Abhari R S and Abreau F 2015 *Extreme Ultraviolet (EUV) Lithography VI* vol 9422 (Bellingham, WA: SPIE Press) p 94222K

[186] Sakabe S, Mochizuki T, Yamanaka T and Yamanaka C 1980 *Rev. Sci. Instrum.* **51** 1314

[187] Jung D *et al* 2011 *Rev. Sci. Instrum.* **82** 013306

[188] Krems M, Zirbel J, Thomason M and DuBois R D 2005 *Rev. Sci. Instrum.* **76** 093305

[189] Bodewits E, Hoekstra R, Dobes K and Aumayr F 2014 *Phys. Rev.* A **90** 052703